Supplementary information

Sodium clusters-driven safety concerns of sodium-ion batteries

Jiaping Niu,‡[ab] Junyuan Dong,‡[ab] Xiaohu Zhang,‡[a] Lang Huang,*[ac] Guoli Lu,[a] Xiaolei Han,[a] Jinzhi Wang,[a] Tianyu Gong,[a] Zheng Chen,[ac] Jingwen Zhao*[ac] and Guanglei Cui*[abc]

[a] Qingdao New Energy Shandong Laboratory, Qingdao Institute of Bioenergy and Bioprocess Technology, Chinese Academy of Sciences, Qingdao 266101, China

[b] Center of Materials Science and Optoelectronics Engineering, University of Chinese Academy of Sciences, Beijing 100049, China

[c] Shandong Energy Institute, Qingdao 266101, China.

‡ These authors contributed equally: Jiaping Niu, Junyuan Dong, Xiaohu Zhang.

*E-mail: huanglang@qibebt.ac.cn; zhaojw@qibebt.ac.cn; cuigl@qibebt.ac.cn

Materials and Methods

Electrodes and Electrolytes. Sodium vanadium phosphate (NVP) power was procured from Guangshui Ennaiji New Energy Co., Ltd. Layer oxide powder was procured from Jiangsu Xiangying New Energy Technology Co., Ltd. Hard carbon (HC) was purchased from Aekyung Petrochemical Co. Ltd. Soft carbon (SC) was obtained from Stanford Advanced Materials (SAM). Ethylene carbonate (EC), diethyl carbonate (DEC), fluoroethylene carbonate (FEC) and sodium hexafluorophosphate ($NaPF_6$) were obtained from Tokyo Chemical Industry Co., Ltd. All electrolytes were prepared in an argon-filled glovebox with moisture and oxygen contents less than 0.01 ppm. All chemicals were used as received without further purification.

Preparation of coin cells and pouch cells and formation test. The HC electrodes for coin cells were fabricated by blending HC, Super P (Hefei Kejing Materials Technology Co., Ltd), sodium carboxymethyl cellulose (CMC, Macklin) and styrene butadiene rubber (SBR, Macklin) in a mass ratio of 95:5:3:2. Similarly, the NVP electrodes were produced by combining NVP, Super P, and PVDF (Suzhou Zhongyan Chemical Technology Co., Ltd) at an 8:1:1 mass ratio. Both slurries were then applied to an Al foil current collector using blade coating and subsequently dried under vacuum at 60 °C for 24 hours. Then, the NVP/HC cells were assembled using polypropylene (PP) separator (ND16, SK Innovation Co., Ltd) and 80 uL 1 M $NaPF_6$ ECDEC (3:7, v/v) in an Ar-filled glove box (H_2O and O_2 < 0.1 ppm). NVP/HC pouch cells with a capacity of 0.9 ~ 1 Ah were assembled using nine pieces of NVP (14.4 mg/cm^2, 60 mm^2 × 80 mm^2) as the cathode, ten pieces of HC (6.57 mg/cm^2, 62 mm^2 × 82 mm^2) as the anode. LFP/graphite pouch cells with a capacity of 0.9 ~ 1 Ah were assembled using five pieces of LFP (20.7 mg/cm^2, 60 mm^2× 80 mm^2, Hefei Kejing Materials Technology Co., Ltd) as the cathode, six pieces of graphite (9.65 mg/cm^2, 62 mm^2 × 82 mm^2) as the anode. All pouch cells were assembled using a "Z" stacking method and conducted in a low-dew-point environment (< −50 °C). All coin cells are tested using a LAND system from Wuhan LAND Electronics Co., Ltd, while all pouch cells are tested with Neware from Shenzhen Neware Electronics Co., Ltd.

For coin cells, the formation is completed directly by two cycles at a rate of 0.1 C. Pouch cells are clamped with two glass plates to force the gas generated during battery formation into the pouch bag. Then, the pouch cells are placed at 40 °C at 0% SOC for 24 hours to allow the electrolyte to fully saturate the electrodes. Next, the pouch cells are transferred to a room temperature control box and charge it at a rate of 0.1 C to 3.7 V for NVP (3.8 V for LFP, 3.95 V for layered oxide), maintaining a constant voltage for 15 minutes, and then discharge them at a rate of 0.1 C to 1.0 V for NVP (2.5 V for LFP, and 2.0 V for layered oxide). Finaly, a secondary vacuum final sealing machine

is used to exhaust and reseal the swollen pouch cells, completing the entire formation process.

General measurements. The ARC tests used ARC BTC500 (HEL, England) instrument. The "heat-wait-search" model starting temperature was 50 °C with a heating step of 5 °C. The detected self-heating rate was 0.02 °C/min and thermal runaway criteria was 1 °C/min. DSC is measured via NETZSCH DSC 200F3. Approximately 5 mg sample is capsuled in a 40 mL gold-coated stainless-steel crucible. A scan rate of 5 ˚C/min is employed under N_2 atmosphere and the temperature is ramping from 0 ˚C to 400 ˚C. Lab XRD measurements are carried out using a Rigaku Smart Lab X-ray diffractometer with Cu Kα radiation. The diffraction data are collected with a step width of 2° over a 2θ range of 10° to 70°. In-situ XRD with an external direct heating component from room temperature up to 400 °C at a heating rate of 1°C/min, was tested from 10° to 70° with a scan speed of 20°/min. SEM images were taken by S-4800 field emission SEM (Hitachi, Japan), operated at 10 kV and element mapping test was conducted by 7593-H (Horiba, Japan). XPS experiments were performed on a Thermo ESCALAB 250Xi instrument equipped with a monochromatic Al Kα X-ray source. High-resolution transmission electron microscopy (HRTEM), HC electrodes were first dispersed in ethanol by ultrasonication and loaded onto a carbon-coated copper grid for imaging on a FEI Tecnai F30 with an acceleration voltage of 300 kV. Liquid ^{1}H NMR measurement was carried out on a Bruker AVANCE III 400 MHz using DMSO-d_6 as solvent. Inductively coupled plasma atomic emission spectrometry (ICP-AES) used a thermo ICS5000 with a conductivity detector. The columns used are Thermo Dionex IonPac AS11-HC 4.0×250 mm. The eluent for anion is 25 mM NaOH with 1 ml/min flow and 25 μL. In addition, the instrument is equipped a suppression, WLK-10A-HJ for anions and the current is 70 mA. Ion Chromatography was conducted on a shimadzu ICPMS-2030 Series. The spray chamber is cooled at 5 °C to ensure temperature stability and to reduce the water vapor present in the nebulizer gas flow. The operation conditions are 1.2 kW high frequency power, 1.1 L/min auxiliary gas flow, 8.0 L/min plasma gas flow, 6.0 ml/min collision gas (Helium) flow. Liquid chromatography–mass spectrometry measurement was performed with mobile phase are acetonitrile and water, chromatographic column is C18 column.

Solid-state NMR measurements. ^{23}Na and ^{7}Li MAS solid-state NMR measurements were performed on a Bruker AVANCE NEO 500WB spectrometer operating at frequencies of 500.130 MHz for ^{1}H, 132.3 MHz for ^{23}Na and 194.37 MHz for ^{7}Li, equipped with a 3.2 mm magic angle spinning (MAS) probe. ^{23}Na and ^{7}Li chemical shifts were referenced with respect to a and 1 M NaCl solution (0 ppm) and 1 M LiCl solution (0 ppm), respectively. The magic angle was calibrated with KBr side bands,

and the samples were spun at 5 kHz in a 3.2 mm equipped with Kel-F caps. To prevent contamination from encountering oxygen, battery disassembly and rotor loading operations were performed in an argon glove box (H_2O and O_2 < 0.01 ppm). Single-pulse MAS ^{23}Na measurements were performed at room temperature at 10 kHz rotation speed using a 4.0 μs π/2 pulse length with an RF field strength of 76.6 kHz, a 5 s recycle delay, and 100 transients. Single-pulse MAS ^{7}Li measurements were performed at room temperature at 15 kHz rotation speed using a 1.75 μs π/2 pulse length with an RF field strength of 76.6 kHz, a 5 s recycle delay, and 50 transients. Spin-lattice relaxation time (T_1) was determined using saturation recovery experiments at varied temperatures.

SI Figures and Tables

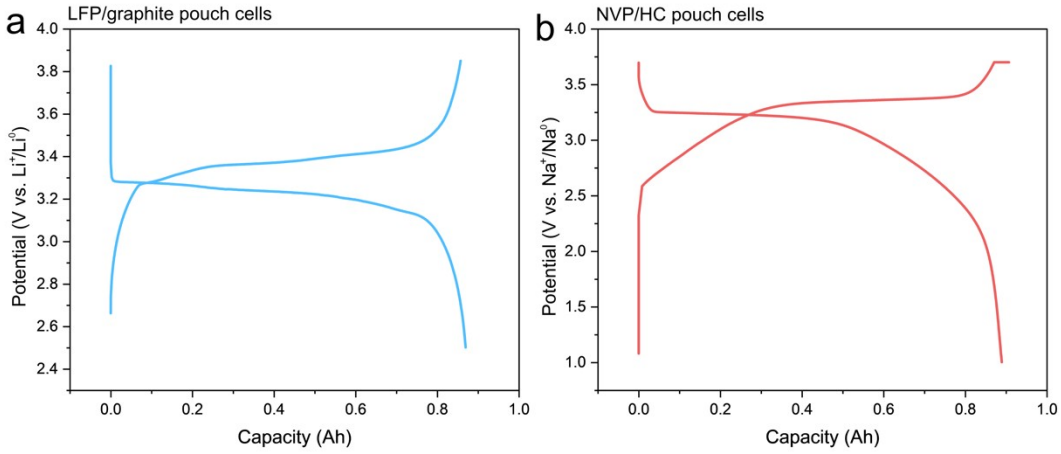

Figure S1. Electrochemical characterization of pouch cells with different configuration. (a) 1 Ah lithium-ion LFP/graphite and (b) 1 Ah sodium-ion NVP/HC pouch cells.

The pouch cells underwent a preliminary formation process, being subjected twice to a cycling rate of 0.1 C to facilitate the SEI formation, followed by a cycling rate at 0.2 C for the ensuing experimental evaluations. A characteristic electrochemical profile suggests that the battery is functioning within optimal parameters.

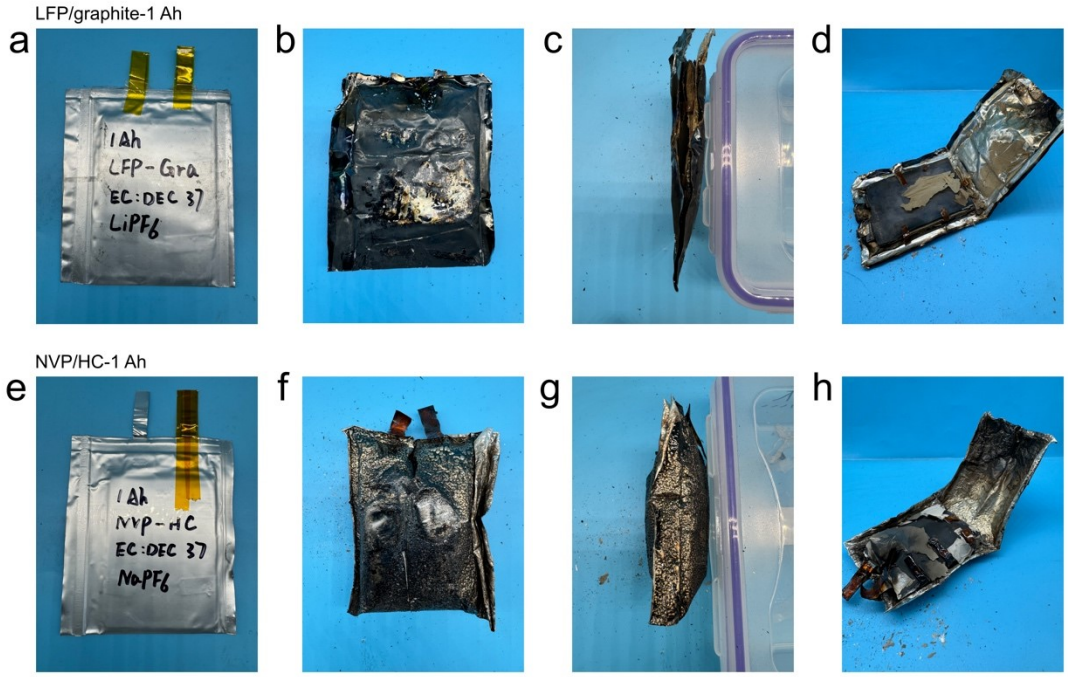

Figure S2. Typical images of the Ah-grade pouch cells before and after ARC tests. Charged lithium-ion LFP/graphite pouch cell before test (a), and front view (b), side view (d), internal view (d) after failure. Charged 1 Ah sodium-ion NVP/HC pouch cell before test (e), and front view (f), side view (g), internal view (h) after failure.

After thermal runaway, the surface morphology of Ah-grade sodium-ion pouch cell and lithium-ion pouch cell exhibited profound destruction. Comparative analysis reveals that sodium-ion pouch cell exhibit a more aggressive explosion than that of lithium counterpart.

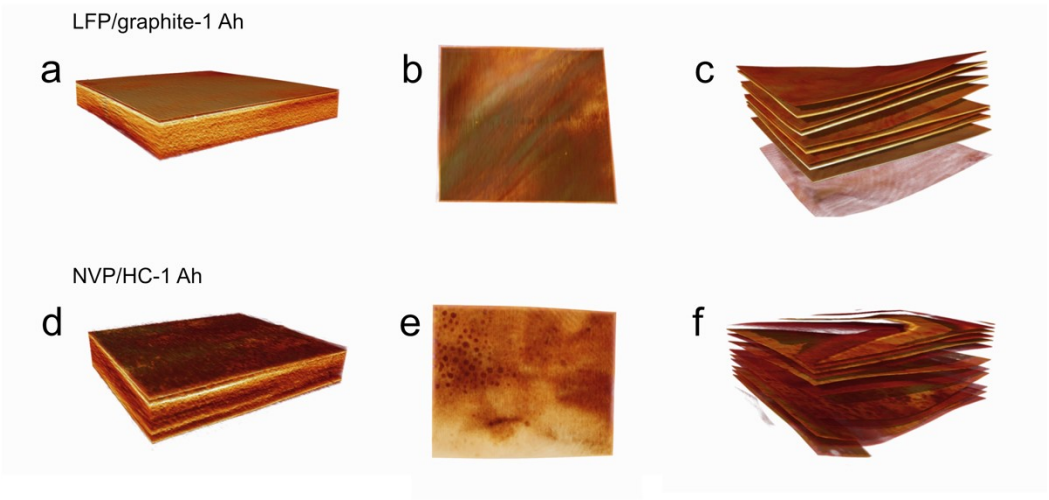

Figure S3. Computed tomography (CT) imagery of the LIB and SIB pouch cells before and after ARC tests. 1 Ah lithium-ion LFP/graphite pouch cell before failure (a), and top view (b), front view (c) after failure. 1 Ah sodium-ion NVP/HC pouch cell before failure (d), and top view (e), front view (f) after failure.

CT images reveal that thermal runaway process violently damaged the inner structures of the pouch cell, and SIBs suffer severer gassing and explosion to twist the electrode layer apart than that of LIBs.

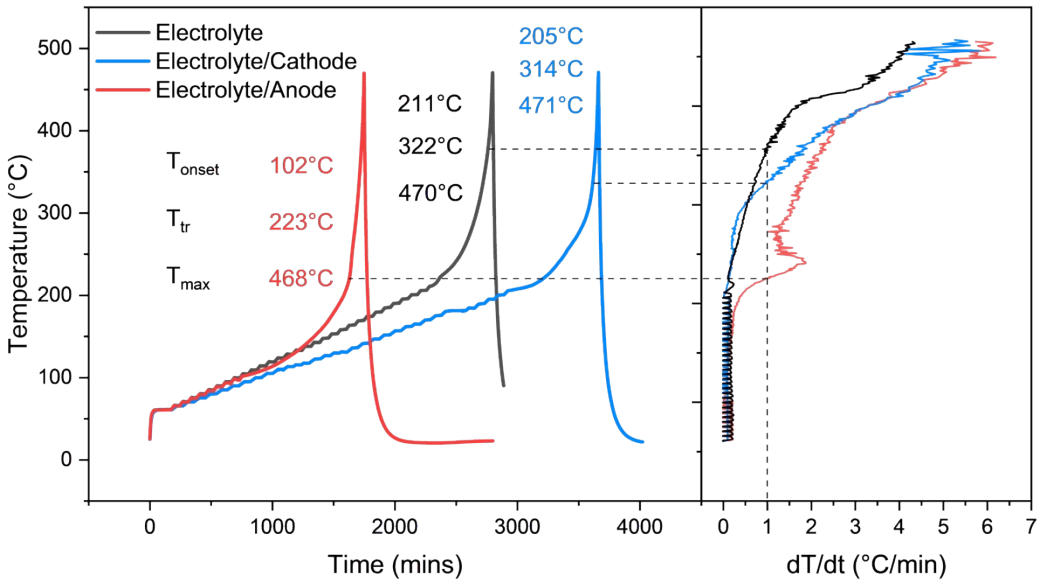

Figure S4. The HWS curve and self-exothermic rate of electrolyte, electrolyte/cathode and electrolyte/anode collected from fully charged NVP/HC pouch cells.

T_{onset} and T_{tr} of the electrolyte/anode combination occurred at earlier temperatures by nearly 100 °C compared to the other two, which agree well with the thermal runaway parameters of sodium-ion pouch cell. This indicates the interfacial reaction between electrolyte and anode is vigorous and dangerous, dominating the overall thermal runaway of the battery.

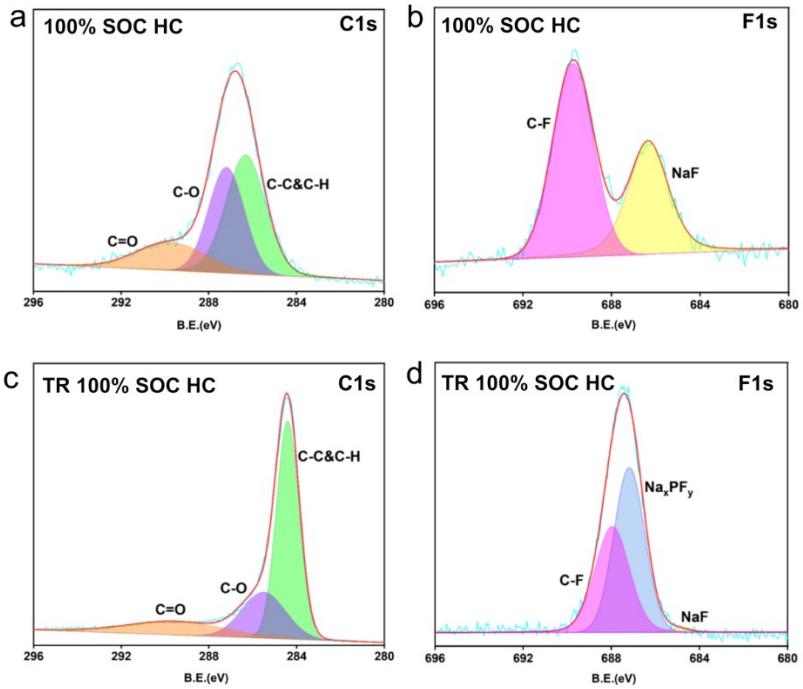

Figure S5. X-ray photoelectron spectroscopy (XPS) C1s for 100% SOC HC (a) and thermal runaway (TR) 100% SOC HC (c). F1s spectra of 100% SOC HC (b) and TR 100% SOC HC (d).

The content of C-O and C=O bonds are reduced after thermal runaway, accompanied by the thermal decomposition of materials. From the perspective of F element, many Na_xPF_y species are generated, which are decomposition products of sodium hexafluorophosphate ($NaPF_6$).

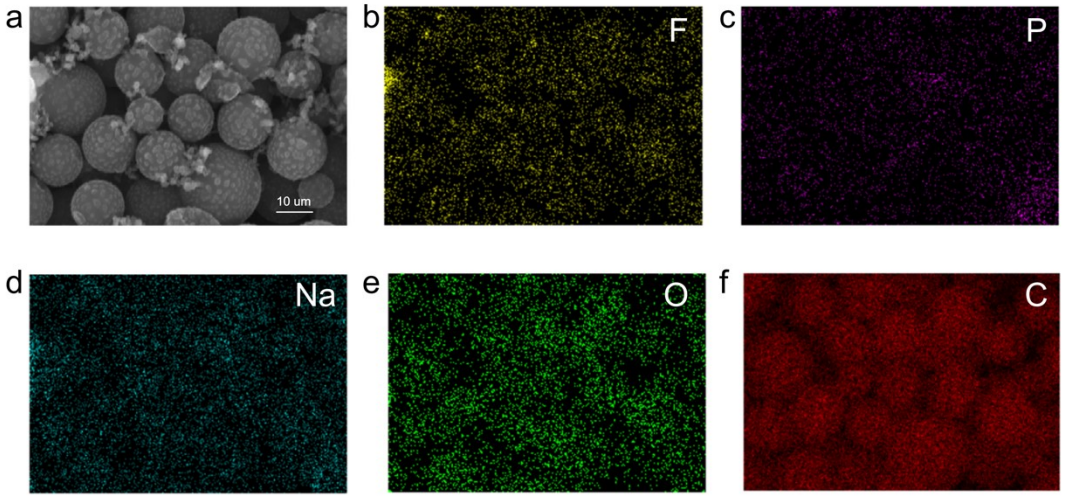

Figure S6. SEM image (a) and element mappings (b) F, (c) P, (d) Na, (e) O and (f) C of TR 100% SOC HC.

After thermal runaway, sodium, fluorine, and phosphorus elements were observed on surface of HC, which is consistent with the Na_xPF_y substance results mentioned above.

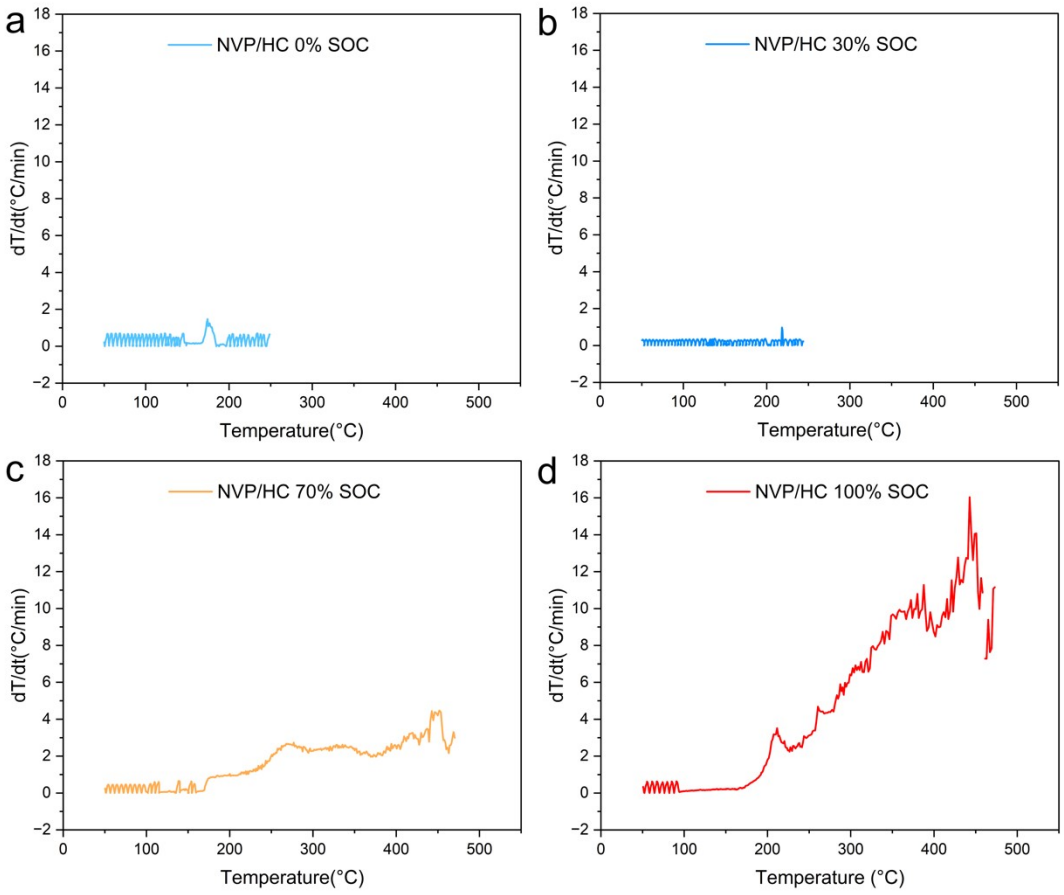

Figure S7. The self-heating rate comparison of NVP/HC with 0% (a), 30% (b), 70% (c) and 100% (d) SOC states.

The pouch cells at 0% SOC and 30% SOC showed almost no heat release, demonstrating good thermal stability. However, 70% SOC and 100% SOC exhibited intense heat release behavior. Although their initial self-heating release temperatures are similar, the amount of heat release at 100% SOC is significantly severer.

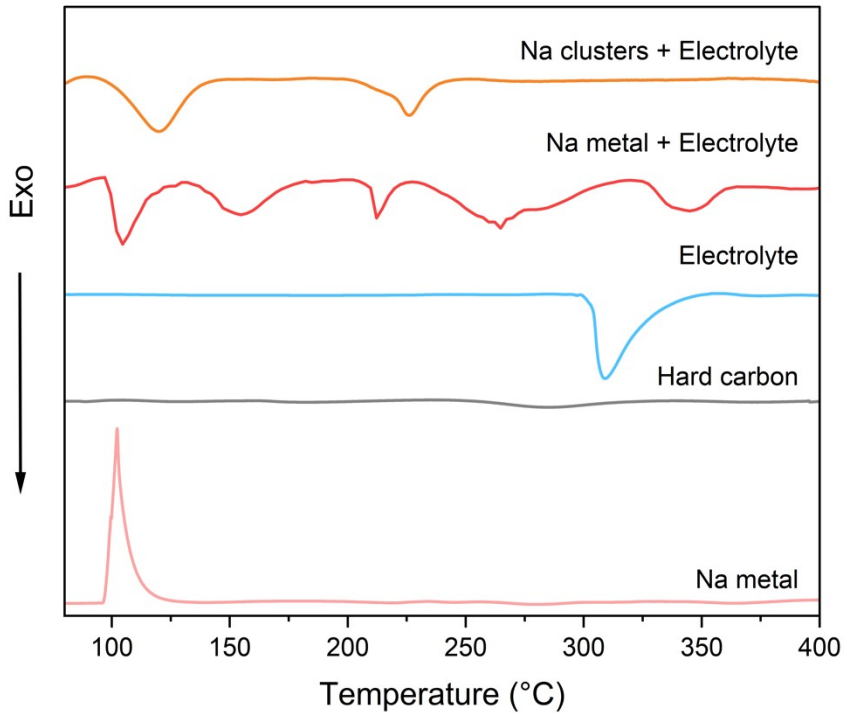

Figure S8. DSC curves of Na clusters/Electrolyte, Na metal/Electrolyte, Electrolyte, Hard carbon and Na metal alone.

it can be observed that the thermal properties of single-component materials exhibit a high degree of uniformity and standardization. The electrolyte undergoes a pronounced exothermic decomposition reaction at 300°C, while hard carbon shows no reaction below 400°C. Pure sodium metal undergoes a melting phase transition at 98°C, characterized by an endothermic behavior. The initial reaction (92 °C) between sodium metal and the electrolyte are strikingly similar to those between sodium clusters and the electrolyte. However, the DSC curve for sodium metal and the electrolyte is more complex, displaying additional exothermic peaks. This is attributed to the significantly larger quantity of sodium metal compared to sodium clusters, an unavoidable phenomenon during the experiment. In terms of initial thermal reaction characteristics, the behavior of sodium clusters is nearly identical to that of sodium metal.

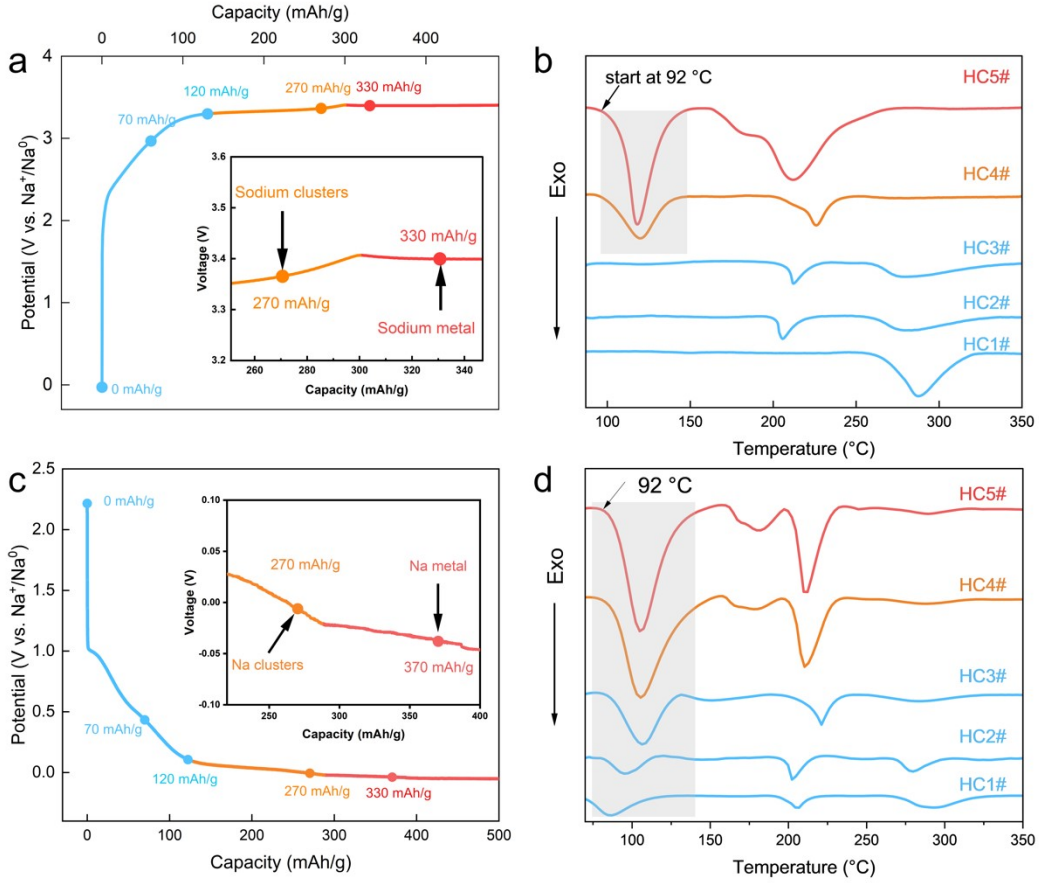

Figure S9. A comparative analysis between sodium ion full cells and half cells. (a) Electrochemical curves of NVP/HC full-cells. (b) DSC curves of HC collected from NVP/HC full-cells. (c) Electrochemical curves of Na/HC half-cells. (d) DSC curves of HC collected from Na/HC half-cells.

Fig. 2 mentions the employment of NVP as the counter electrode. Here, changing the counter electrode to sodium metal, we are surprised to find that the third point HC3#, which theoretically does not have sodium clusters, also showed an obvious 92°C exothermic peak on the DSC curve. It is speculated that the presence of sodium metal counter electrode directly leads to the reduction of electrolyte during cycling of the battery, indicating that the existence of metallic sodium could trigger the exothermic reactions.

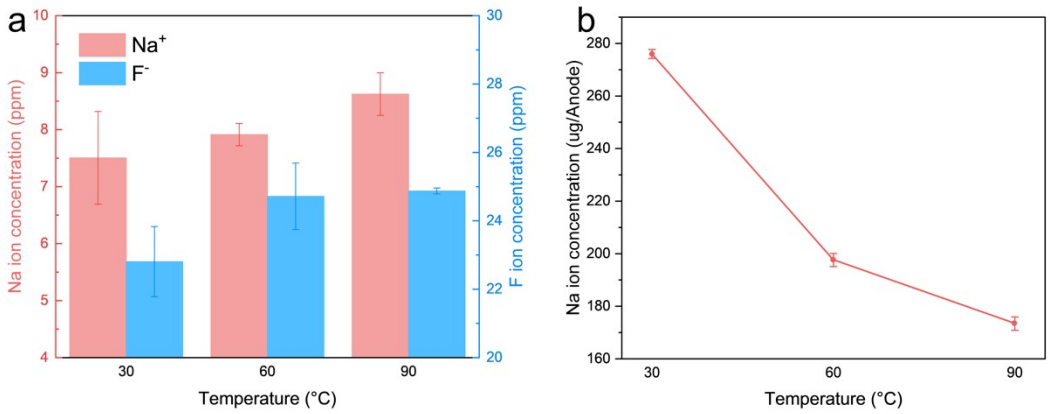

Figure S10. Evaluation of SEI thermal stability in SIB. (a) Sodium and fluoride ions content in the electrolyte under heating treatments. (b) Remaining sodium ions content on the electrode.

Sodium coin cells were assembled and cycled three times to ensure the formation of a stable SEI at the anode. Following this cycling process, the sodiated HC electrodes were collected. These electrodes were then immersed in a fresh electrolyte and maintained at constant temperatures of 30°C, 60°C, and 90°C for a duration of 3 hours. The supernatant was taken out and fluoride ion content was detected by ion chromatography, and sodium ion content was studied by inductively coupled plasma optical emission spectroscopy (ICP-OES). The electrode was performed microwave ablation for ICP test to measure the remaining sodium ion content. The concentration of sodium and fluoride ions within the electrolyte exhibits a marked elevation concomitant with rising temperatures, whereas the content of sodium ions within the electrode demonstrates a conspicuous decline. This observation suggests that the SEI in SIBs exhibits thermal instability, undergoing progressive degradation at elevated temperatures. Consequently, this leads to the absence of a marked exothermic peak for SEI rupture in DSC curve.

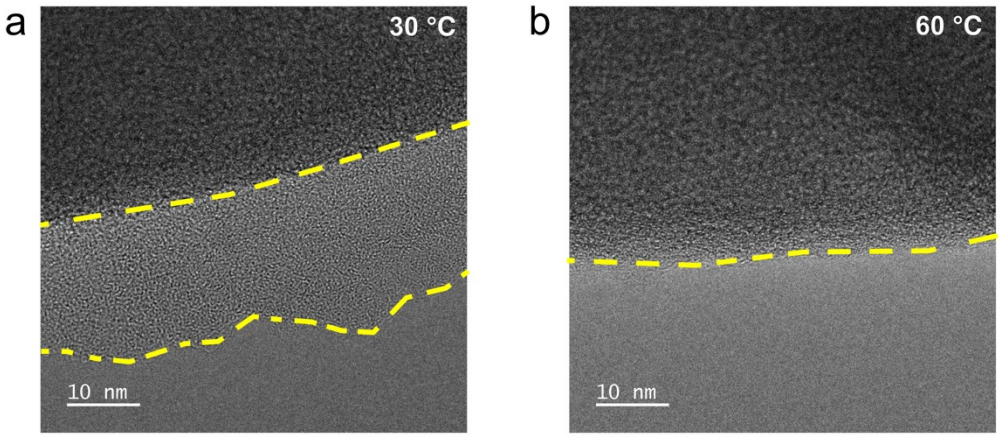

Figure S11. Transmission electron microscopy (TEM) images of HC electrodes before (30 °C) and after (60 °C) soaking heat treatment.

To further elucidate the susceptibility of the SEI to thermal degradation, the fully charged HC anode was submerged within the electrolyte milieu and subjected to thermal treatment within ovens set at 30°C and 60°C, respectively, for a duration of one hour. Subsequent observation under TEM revealed that the SEI structure exposed to the lower temperature remained largely intact, whereas the SEI under the elevated temperature of 60°C exhibited near-complete disintegration. These findings underscore the thermal vulnerability of the SEI in SIB.

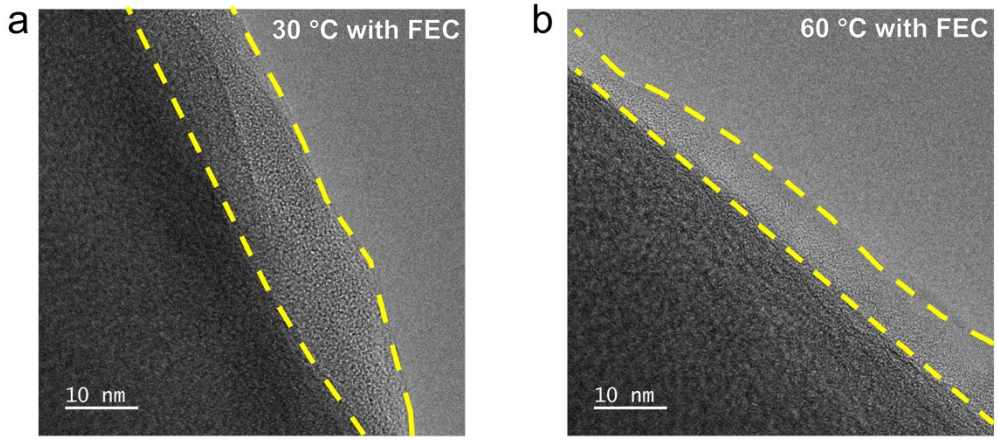

Figure S12. Transmission electron microscopy (TEM) images of HC electrodes FEC addtive before (a, 30 °C) and after (b, 60 °C) soaking heat treatment.

Incorporating the SEI film-forming agent fluoroethylene carbonate (FEC) into the 1M $NaPF_6$ in EC:DEC (3:7), the HC electrodes were subjected 1 hour thermal insulation experiments at 30 °C and 60 °C in electrolyte milieu. It was observed that the structural integrity of the SEI components at both temperatures remained preserved. This phenomenon suggests that the integration of FEC markedly enhances the heat resistance of the SEI in SIB.

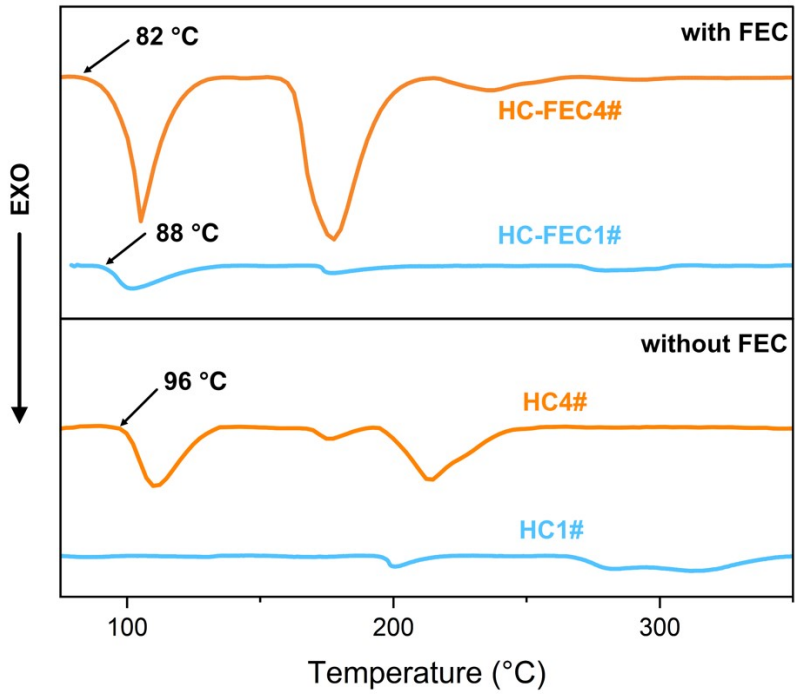

Figure S13. DSC curves of HC electrodes with and without FEC additive.

HC1# (0% SOC HC under the base electrolyte milieu) does not show any exothermic peaks within 200 °C. Based on the results of the Fig. S9 and Fig. S10 experiments, SEI gradually dissolves during the heating process, making it difficult to show exothermic peak of SEI rupture. However, HC4# undergoes strong interfacial reactions with the electrolyte due to the presence of sodium clusters, and shows a clear exothermic peak at 96 °C. The incorporation of the interlayer-forming agent FEC augments the thermal resistance of the SEI, as evidenced by the detection of an exothermic peak at 88 °C for HC-FEC1#. When sodium clusters are presented, the exothermic peak was further decreased to 82 °C, indicating that the SEI formed by FEC cannot effectively prevent the reaction between sodium clusters and electrolyte. The above results indicate that once sodium clusters are formed, they will always advance the exothermic reaction between the anode and electrolyte, posing a huge safety hazard to SIBs.

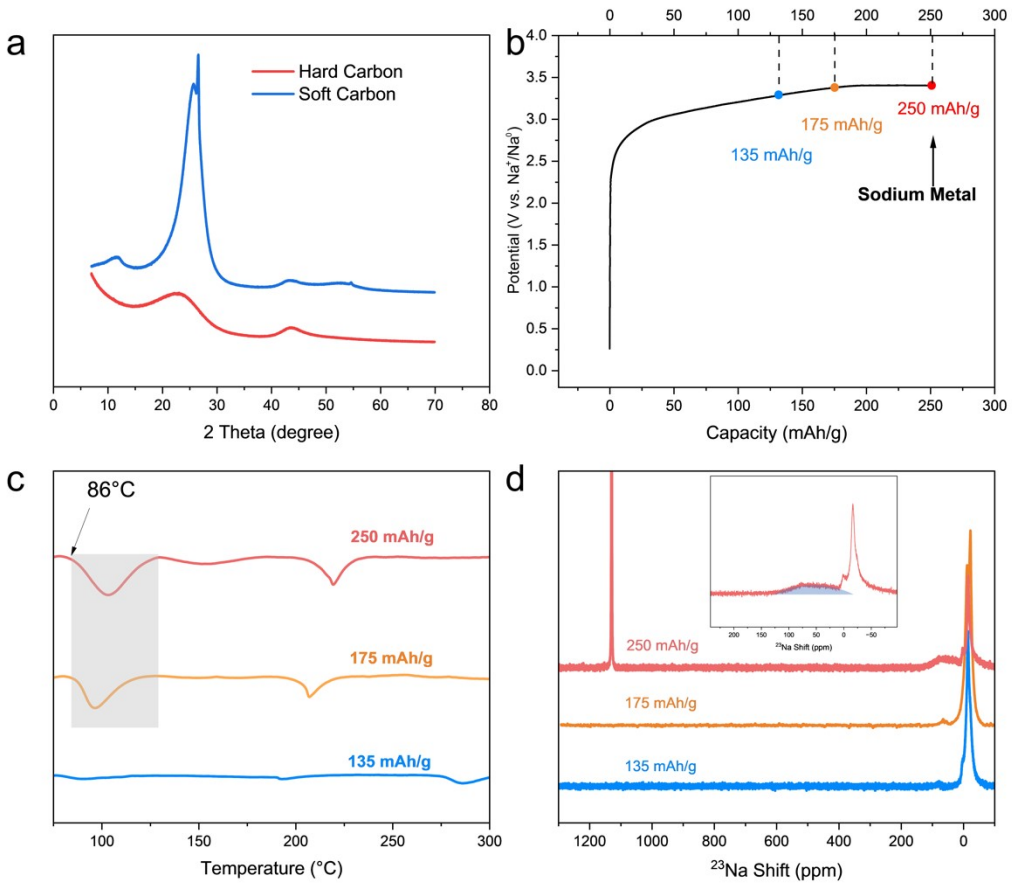

Figure S14. Performance of sodium clusters in soft carbon. (a) XRD patterns of HC and SC. (b) Electrochemical curve of SC. (c) DSC curves of SC anode materials with 135 mAh/g, 175 mAh/g and 250 mAh/g. (d) MAS ^{23}Na spectra of SC.

For carbon materials, carbon with disordered structure difficult to eliminate at high temperature (2800°C) is called hard carbon (HC), while those with disorder structure that can be easily eliminated is called soft carbon (SC). The difference between them lies in the arrangement of their internal carbon layers. As shown in the fig. 13a, the intensity of (002) diffraction peak for SC is higher than that of HC, while the in-plane diffraction peak (110) is similar. This suggests that SC is more crystalline than HC in the stacking direction, implying a narrower layer space as well as larger crystallite size, whereas the in-place crystallinity is similar. As a result, the true density of the SC is higher than that of the HC, reflecting the smaller microporous structure of the former.

As for the electrochemical curve (Fig. S13(b)), the SC only shows a monotonically slope followed by sodium metal deposition, without a pattern similar to the HC plateau

region. Therefore, it is difficult to form sodium clusters in SC. We assembled coin cells of NVP/SC 1M $NaPF_6$ in EC:DEC (3:7) to further explore the relationship between sodium clusters and exothermic behaviors, and three points (135 mAh/g, 175 mAh/g and 250 mAh/g) were selected for NMR and DSC tests.

No sodium clusters signal was evident in NMR plot for sample collected at 135 mAh/g, while an additional bulge peak in the range from 20 ppm to 100 ppm, which was distinguish from those of ordinary ionic sodium signals, was observed both for samples of 175 mAh/g and 250 mAh/g. Considering that the chemical shift of sodium clusters is directly related to the hole size and charge of state, we speculate that SC can also generate sodium clusters with a certain size in closed pores at the end of the slope capacity. Due to the inherent characteristics of SC, which has a high true density and small pores, it is impossible to form sodium clusters of a similar size as in HC, so the intensity of sodium clusters in the SC is much lower, and the chemical shifts are more upfield. The DSC result also confirmed this result. No early exothermic peak was observed for sample from 135 mAh/g. In contrast, sample from 250 mAh/g showed an exothermic peak starts at 86 °C. Excitingly, an identical exothermic peak also emerged at early stage for sample of 175 mAh/g, which is in presence of sodium clusters but without depositing sodium metal, demonstrating that sodium clusters in SC with small size can also trigger the onset interfacial exothermic reactions.

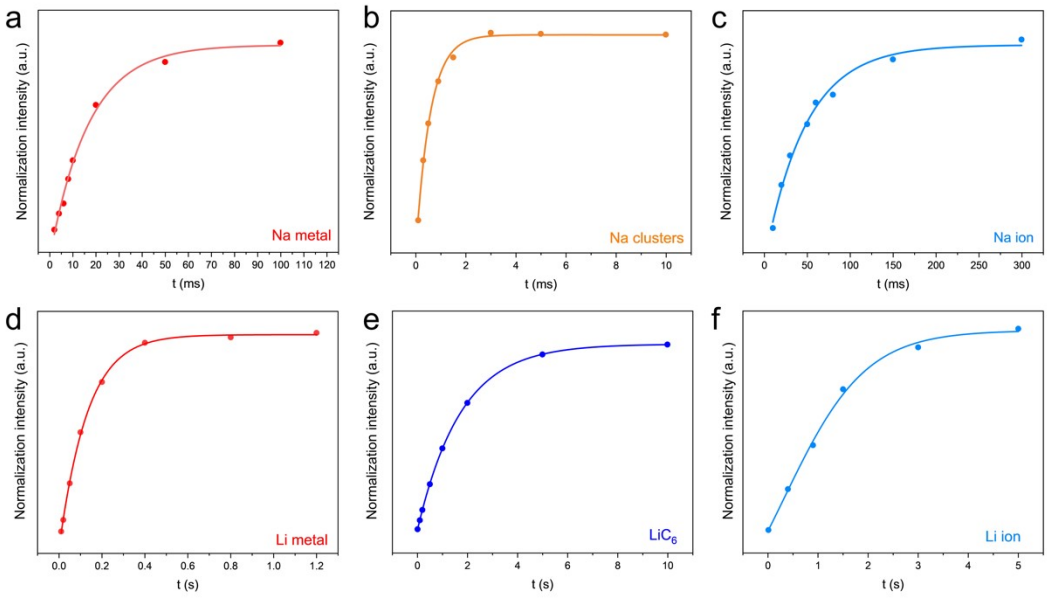

Figure S15. Spin-lattic relaxation (T_1) processes of sodium ion (a), sodium clusters (b), sodium metal (c), lithium ion (d), LiC_6 (e) and lithium metal (f) at room temperature.

Spin-lattice relaxation describes the process by which the energy in a spin system returns to thermal equilibrium through interaction with the surrounding lattice (i.e., the vibrational states of atoms or molecules), providing information about the molecular environment and dynamics. In this article, we measured the spin-lattice relaxation time using the saturation recovery method. Initially, the population distribution among all energy levels in the system is saturated by radiofrequency pulses, nearly eliminating the population difference between the high and low energy states. After stopping the irradiation, the spin system will begin to exchange energy with the surrounding environment and gradually return to thermal equilibrium. By measuring the rate of change in net magnetization over time (i.e., the recovery rate), the T_1 relaxation time can be determined.

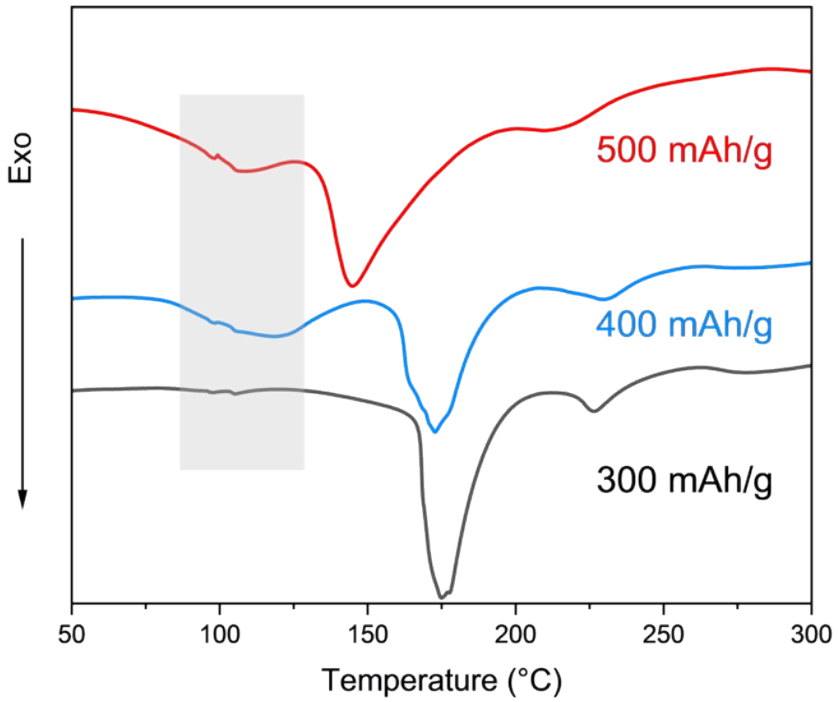

Figure S16. Metallic sodium is responsible for causing massive heat generation. DSC curves of HC with 300 mAh/g, 400 mAh/g and 500 mAh/g capacity.

Excess sodium atoms are embedded into the HC electrodes, and the capacity exceeding 300 mAh/g is contributed by the sodium metal plating on the surface of the HC. As the content of metallic sodium (including sodium clusters and sodium metal) in the system increases, the enthalpy of the exothermic peak near 90 °C augmented. Meanwhile, the exothermic peak located 175 °C at 300 mAh/g capacity also downshifted to 140 °C at 500 mAh/g. It is worth noting that the increase in metallic sodium content did not trigger new exothermic peaks, indicating that sodium clusters and sodium metal are structurally analogous, and the type of exothermic reactions they trigger remains consistent. Concurrently, this also elucidates that sodium clusters are intrinsically linked to the thermal runaway temperature of the battery (a rapid exothermic reaction), underscoring the pivotal role they play in determining the thermal stability of the system.

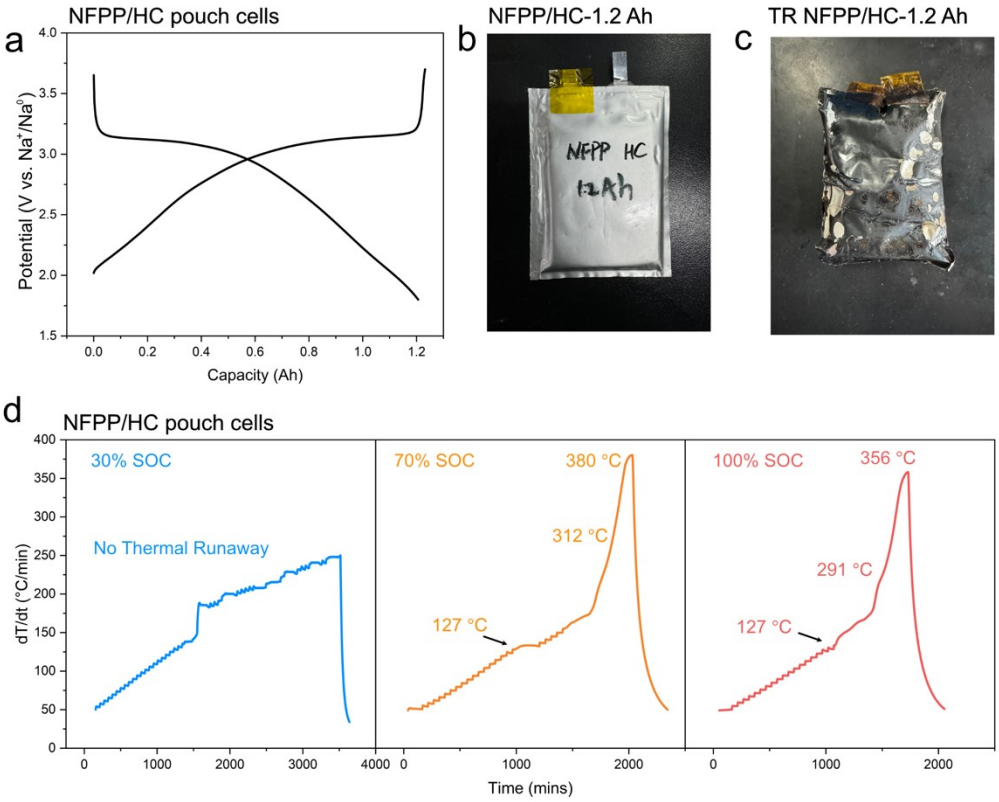

Figure S17. Therma runaway behavior of NFPP/HC pouch cells. (a) Electrochemical curve of Ah-grade NFPP/HC pouch cells. NFPP/HC-1.2 Ah pouch cell before (b) and after (c) thermal runaway. Heat-wait-search (HWS) curves (d) with varied SOC states of pouch cells.

NFPP and NVP are both polyanion-based cathodes, both exhibit similar thermal properties. In the absence of sodium clusters, the thermal safety of NFPP/HC-30% SOC is good.

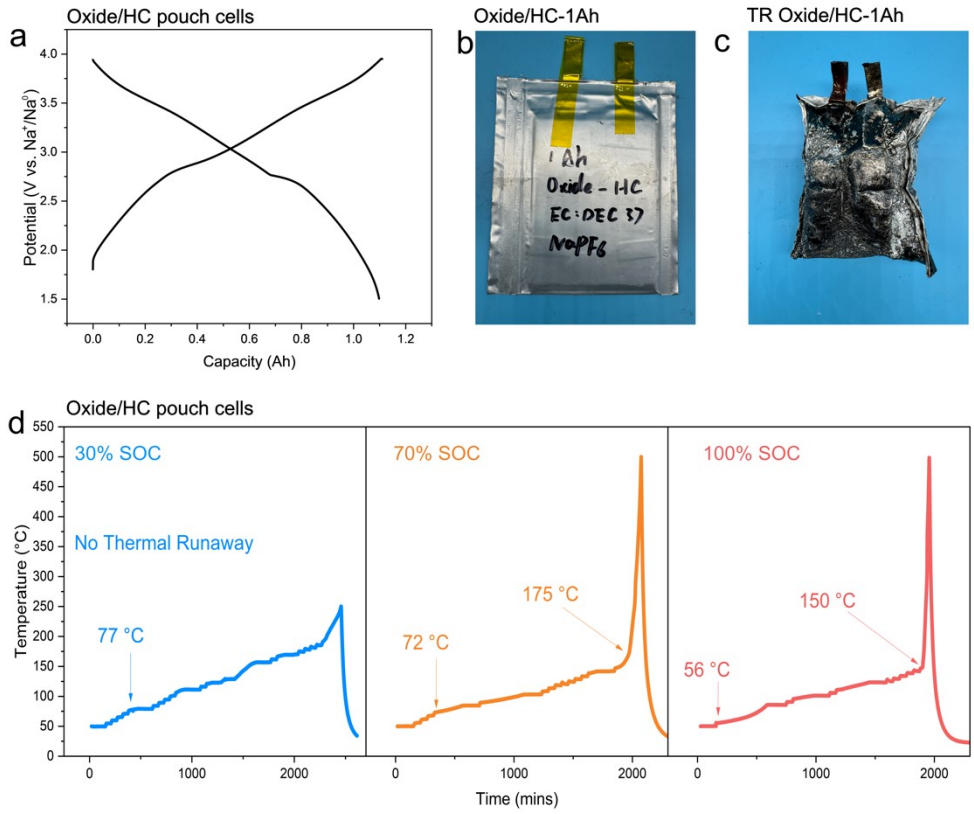

Figure S18. Therma runaway behavior of layered oxide/HC SIB pouch cells. (a) Electrochemical curve of Ah-grade layered oxide/HC pouch cell. Oxide-HC-1 Ah pouch cell before (b) and after (c) thermal runaway. (d) Heat-wait-search (HWS) curves of different SOC states of pouch cells.

The thermal runaway of oxide cathode-based pouch cells involves the dissolution of transition metals and the release of reactive oxygen species, so the thermal runaway mechanism of Oxide/HC pouch cells is different from that of polyanion system sodium-ion pouch cells. The participation of cathode side reactions will further advance the initial exothermic temperature of thermal runaway. However, we still observed a significant difference of the onset self-heating behavior in the 30% SOC and 70% SOC cells, implying the universality that the sodium clusters posing a critical role on determining the thermal safety of sodium batteries.